Endovascular neuromodulation: feasibility of endovascular stimulation near the cerebellum

Journal of Neural Engineering

PAPER

OPEN ACCESS

RECEIVED
1 April 2026

REVISED
12 August 2026

ACCEPTED FOR PUBLICATION
13 August 2026

PUBLISHED
26 August 2026

Endovascular neuromodulation: feasibility of endovascular stimulation near the cerebellum

Weijie Qi[1,*], Joel Villalobos[1,2], Jingyang Liu[3], Huakun Xin[1], Martin J Spencer[1], Sepehr Kazemi[1], Stella Ho[1], Joseph West[4], David B Grayden[1,2] and Sam E John[1,2]

[1] Department of Biomedical Engineering, The University of Melbourne, Melbourne, Australia
[2] Graeme Clark Institute, The University of Melbourne, Melbourne, Australia
[3] Vagus Nerve Stimulation Centre of Excellence, Bionics Institute, Melbourne, Australia
[4] School of Computing and Information Systems, The University of Melbourne, Melbourne, Australia
[*] Author to whom any correspondence should be addressed.

E-mail: james.qi@unimelb.edu.au

Keywords: endovascular neuromodulation, cerebellar stimulation, cortical evoked potentials, stent-electrode array

Supplementary material for this article is available online

Abstract

Objective. Electrical stimulation and neural recording underpin neural prostheses for restoring function and treating neurological disorders, but clinical adoption is limited by the invasiveness of implantation. The Endovascular Neural Interface offers an alternative by accessing intracranial targets through the cerebral vasculature. This work presents the first strength-duration characterization of cortical evoked potentials, elicited by endovascular stimulation, adjacent to the cerebellum. *Approach.* A polymer-based stent-electrode array was deployed into the left transverse sinus of an ovine model. Biphasic current pulses targeting the cerebellum were delivered via the stent electrodes. Cortical responses were recorded using a subdural electrocorticography grid. *Main results.* Endovascular stimulation consistently evoked time-locked cortical potentials with early and late components at approximately 40 ms and 100 ms post-stimulation. Electrode functionality and stability were confirmed through impedance monitoring throughout the experiments. Strength-duration analysis revealed rheobase and chronaxie values, providing a quantitative basis for parameter selection and comparison with established intracranial stimulation modalities. *Significance.* These results demonstrate that endovascular electrodes may access non-superficial brain structures and evoke reproducible cortical responses without open neurosurgery. This work helps establish a foundational framework for endovascular neuromodulation and supports further investigation of its potential for future closed-loop and network-level neuromodulation research.

1. Introduction

Electrical stimulation is the foundation of modern neuromodulation, enabling restoration and modulation of neural function in conditions ranging from sensory loss to movement disorders [1]. The long-term success of these therapies depends on stable electrode–tissue interfaces that reliably modulate neural activity while minimizing biological disruption [2]. However, conventional brain stimulation approaches typically require craniotomy and placement of cortical surface or penetrating electrodes, procedures associated with surgical risk, unwanted tissue response, and limitations in accessing deep or posterior brain structures [3–5].

Endovascular neural interfaces have emerged as a minimally invasive alternative, exploiting the cerebral vasculature to access neural circuits without direct penetration of brain tissue. Stent-based endovascular electrodes have demonstrated stable, chronic neural recording with preserved vessel patency, supporting their translational potential [6–8]. Despite this progress, the use of endovascular platforms for therapeutic electrical stimulation, particularly for stimulation with the stent placed adjacent to subcortical or cerebellar structures, remains unexplored.

The cerebellum is an attractive target for neuromodulation due to its extensive connectivity with cortical and subcortical networks, including cerebellothalamocortical motor circuits as well as

projections to prefrontal and limbic regions involved in cognition and emotion. Dysfunction within these circuits has been implicated in movement disorders, epilepsy, stroke-related deficits, and neuropsychiatric conditions, such as major depressive disorder and schizophrenia [9–11]. Despite this therapeutic potential, the cerebellum's deep anatomical location beneath the occipital cortex and its proximity to major venous sinuses present substantial challenges for conventional stimulation techniques [12]. Non-invasive methods are limited by insufficient depth penetration and focality, while surgically implanted electrodes require craniotomy and carry risks of hemorrhage and tissue injury. Endovascular approaches may overcome these limitations by enabling minimally invasive access to vascular structures adjacent to the cerebellum, allowing stimulation near neural tissue without direct parenchymal penetration.

This study presents the first evaluation of endovascular stimulation with endovascular electrodes placed in the transverse sinus adjacent to the cerebellum and visual cortex using a polymer-based stent-electrode array incorporating thin-film electrodes. Using cortico-cortical evoked potential paradigms [13] and strength-duration modeling in an ovine model, we demonstrate that endovascular electrical stimulation can reliably evoke measurable cortical responses. Strength-duration analysis provides quantitative characterization of rheobase and chronaxie, thereby enabling estimation of neural activation thresholds and insight into the underlying electrode-tissue interface dynamics. Such modeling is critical for optimizing stimulation waveform design, improving energy efficiency, and defining safe operating limits for intravascular neuromodulation. Together, these findings establish the stimulation threshold characteristics and interface behavior of endovascular electrodes, advancing this technology toward a feasible and minimally invasive approach for neuromodulation adjacent to the cerebellum.

2. Methods

2.1. Stent electrode array fabrication and characterization

A polyimide-based flat stent (12 mm width × 24 mm length) was fabricated polymer–metal mesh using a sacrificial-release, multilayer photolithographic process on a silicon carrier wafer incorporating five platinum disk electrodes (diameter: 950 μm, surface area: 0.71 mm^2), as shown in figure 1(A). A photodefinable polyimide base layer was patterned and overlaid with a Ti–Au–Pt metal stack defining the electrodes and interconnects, followed by a photodefinable polyimide encapsulation layer with windows opened over the electrode sites. Exposed platinum contacts were roughened by sputtering to lower interfacial impedance [14].

Each electrode was soldered to 33 μm Pt-tungsten wires and secured with UV-curable adhesive. A nickel-titanium shaft was integrated at the distal end to enable deployment via a coaxial catheter system. Wires were helically routed and insulated within a polyethylene (PE) tube to prevent mechanical failure. The proximal ends (distal ends of the wires) were connected to an external stimulator.

Electrode surface morphology and roughness were characterized on 12 electrodes using atomic force microscopy (AFM) and scanning electron microscopy (SEM). SEM imaging was performed using the FlexSEM1000 system with an accelerating voltage of 20 kV, an emission current of 97 μA, and a chamber vacuum pressure of 50 Pa to visualize surface features such as pore structures, coating integrity, and grain boundaries. AFM measurements were conducted in tapping mode using the JPK Nanowizard III BioAFM system to quantify surface roughness within a 4 × 4 μm scan area.

Electrochemical impedance spectroscopy (EIS) was conducted across a frequency range of 1 Hz to 1 MHz under multiple sweeps using 10 μA current to evaluate impedance characteristics of the electrodes using an Interface 1010 Potentiostat [15]. *In vivo* EIS was performed weekly with a two-electrode configuration to confirm electrode viability (WE: stent electrode, CE and REF: ground electrode on the shoulder) [16]. Implanted electrodes were considered functional if impedance at 1 kHz was within 1–30 kΩ and phase angle at 100 Hz was less than 30° [16].

2.2. Stent implantation

Experiments were conducted with approval from the Animal Ethics Committee of The Florey Institute of Neuroscience and Mental Health (AEC Number: 22–010-UM) and in accordance with the Australian Code for the Care and Use of Animals for Scientific Purposes (8th Edition, 2013). Adult Corriedale ewes (n = 6) were anesthetized with 1.5%–2.5% isoflurane. The stent electrode array (5 electrodes each) was deployed into the left transverse sinus via percutaneous jugular vein access under fluoroscopic venographic guidance, using angiographic techniques and a C-arm imaging system [17]. Angiography was used to highlight the road map from the jugular to the transverse sinus. Intraoperative heparin was administered to prevent thrombosis, and antibiotics were provided for three days post-surgery. Electrode position was confirmed using intraoperative fluoroscopy and postmortem dissection. The stent remained implanted for four weeks to allow integration and stabilization of the device within the vessel wall. During this period, animals underwent weekly impedance spectroscopy (EIS) measurements to monitor implant stability and electrode–tissue interface characteristics. Following this implantation

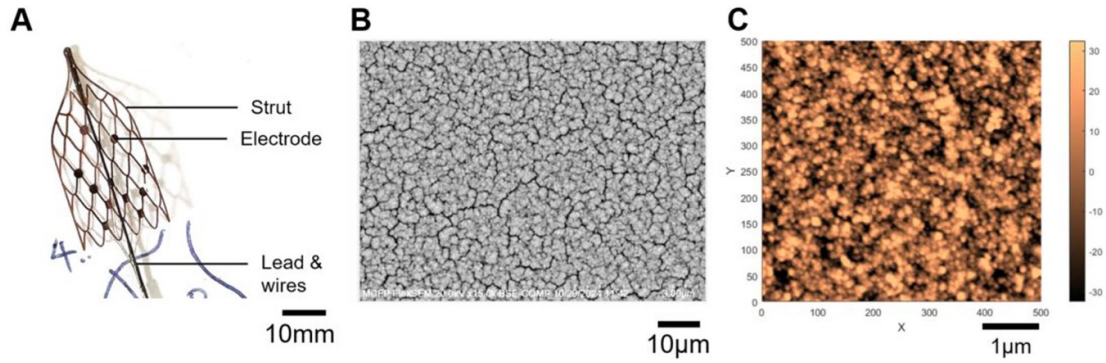

Figure 1. (A) Stent-electrode array designed for implantation in the transverse sinus. The stent struts, electrodes, lead, and connecting wires are indicated by the lines. (B) Scanning electron microscopy (SEM) image of the electrode surface at 15 000× magnification, showing detailed surface morphology. (C) Atomic force microscopy (AFM) image acquired in tapping mode, providing nanoscale topographical information of the electrode surface.

period, terminal acute electrophysiological experiments were performed under general anaesthesia, during which endovascular stimulation and cortical recordings were acquired.

2.3. Electrical stimulation paradigm

Electrical stimulation was delivered under general anesthesia using the Twister stimulator (Dr Langer Medical, Germany) in a common-cathode, charge-balanced biphasic configuration. Stimulation parameters were delivered in a pseudorandom sequence: current amplitudes of 1–4 mA (0.1 mA steps), pulse widths of 100–800 μs (100 μs steps), 100 repetitions per setting, and a 2.01 s interstimulus interval (stimulation frequency of 0.498 Hz), corresponding to a theoretical parameter space of 248 combinations. However, a targeted subset of 104 combinations was selected for testing based on pilot parameter testing. The eyes and ears of sheep were covered to minimize visual and auditory input. All viable electrodes were tested for strength–duration profiling in a single session.

2.4. Acquisition of evoked potential

During the terminal experiments, a craniotomy and durotomy were performed to expose the left cortical hemisphere. A 32-channel electrocorticography (ECoG) grid (CorTec Micro 4 × 8 Square 45°, PtIr electrodes, 1 mm spacing, 1000 μm diameter) was placed on the cortical surface. Anatomical landmarks (e.g. 3 mm anterior to lambda, lateral to the horn) were used to ensure consistent placement. Cortical signals were recorded using the g.tec HiAmp system (g.tec Medical Engineering, Austria) at 4800 Hz sampling rate with cranial screw reference and no hardware filtering. The grid was secured with sutures and screws, and bilateral cranial screws were used as references. ECoG Signals were recorded using g.tec HiSys software and MATLAB Simulink.

2.5. Signal processing

Data were processed offline in MATLAB. Stimulus onset was extracted from a dedicated trigger channel. A 2 ms window before and after each stimulus was blanked to remove artifacts and interpolated with spline interpolation. Signals were then notch filtered at 50 Hz and its harmonics up to 2000 Hz using a second-order Butterworth filter. Band-pass filtering (1–400 Hz) was performed using backward filtering, implemented by reversing the signal, applying forward filtering, and re-reversing the output to avoid post-stimulus distortion. Epochs (−500 to +500 ms relative to stimulus onset) were extracted. Epochs with amplitudes exceeding ±500 μV were commonly associated with stimulation artifact, motion, or amplifier saturation and thus were rejected [18]. Remaining epochs were averaged to obtain evoked potentials. After euthanasia ($\geqslant$10 min post-injection) and following confirmation of absent cortical activity and brainstem reflexes, recordings were repeated to estimate baseline noise and quantify stimulus artifact.

2.6. Data analysis

Evoked potentials were analyzed for positive and negative peaks. Trace plots were generated for each stimulation condition. Activation was defined as peak-to-peak amplitude exceeding 2 times the root mean square (RMS) of the 50 ms pre-stimulus baseline [19]. Strength–duration curves were generated by identifying the minimum current at each pulse width required to evoke a response meeting this criterion. Peak amplitude and latency were quantified for both peaks. RMS and area under the curve (AUC) were calculated within 30–70 ms and 80–120 ms windows to map spatial activation. The spatial distribution of cortical responses was quantified using the AUC-weighted centroid, RMS spatial spread, and the distance between the centroid and the electrode with the maximum AUC. The amplifier channels were mapped to the ECoG layout and co-registered with anatomical data from postmortem dissection.

Random subsets of 30, 50, and 75 epochs were used to assess signal-to-noise ratio (SNR) convergence and correlation with a 75-epoch average. Signal stability was evaluated by comparing responses at the start and end of the recording session. SNR was calculated as

$$\mathrm{SNR} = 20\log_{10}\frac{\mathrm{RMS}_{\mathrm{signal}}}{\mathrm{RMS}_{\mathrm{baseline}}}. \quad (1)$$

3. Results

3.1. Electrode characterization and validation

Figure 1(A) shows the stent electrode array with Pt thin-film electrodes integrated onto the polyimide stent struts. SEM and AFM were performed to capture micro- and nanoscale features, as shown in figures 1(B) and (C), respectively. SEM revealed a continuous and uniform Pt coating with no visible delamination or structural defects. AFM analysis in figure A3 reported a RMS roughness (Rq) of 17.24 ± 2.46 nm and (Ra) of 13.90 ± 1.84 nm ($n = 12$), comparable with a previous study [20]. The electrodes exhibited a porous and textured surface, which serves to increase the electrochemical surface area and charge injection capacity.

EIS was used to characterize the electrochemical interface, revealing a stabilizing impedance profile within the cortical vasculature compared to the degassed saline baseline (figure 2). Phase analysis (figure 2(A)) indicated a less capacitive response *in vivo*, with a phase remaining above −50° at low frequencies compared to approximately −60° in saline. This was accompanied by a lower impedance magnitude and a more gradual frequency roll-off *in vivo* (figure 2(B)), a typical profile with the presence of biological tissue surrounding the electrode [16]. The measured *in vivo* impedance at 1 kHz was below 10 kΩ, which is within the optimal range that support effective neurostimulation and indicative of stable tissue integration four weeks post-implantation.

3.2. Electrode implantation verification

Accurate deployment of the stent-electrode array was confirmed using digital subtraction angiography (DSA) and postmortem anatomical examination. As shown in figure 3(A), the stent was successfully navigated from the jugular vein into the transverse sinus using a catheter guided by a J-wire. The device was positioned adjacent to the cerebellum within the transverse sinus. DSA verified vessel patency, confirming the absence of vascular obstruction following implantation. Postmortem examination following stimulation protocol confirmed the final optimal location of stent-electrode array and ECoG array. As shown in figure 3(B), the stent remained securely in place along the left transverse sinus, with preserved venous patency and surrounding anatomical structures. Figure 3(C) shows the subdural ECoG array

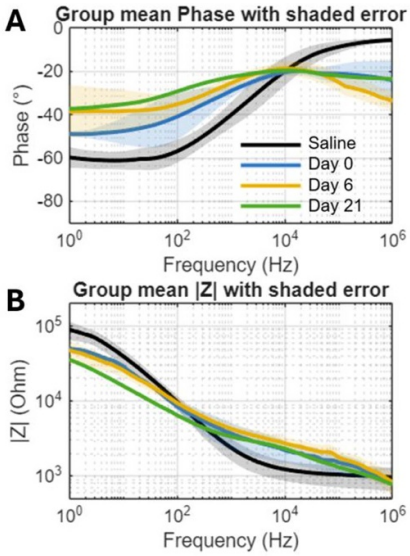

Figure 2. Electrochemical impedance spectroscopy (EIS) results comparing (A) mean phase and (B) mean impedance magnitude for *in vivo* (blue, yellow, and green lines) versus *in vitro* (black line) environments from 3 stent implants (10 electrodes). Shaded areas denote standard deviations ($n = 10$).

positioned directly over the motor cortex, enabling verification that recorded signals originated from the targeted cortical region. These findings support the brain signal origin and precise implantation via the cortical venous system.

3.3. Evoked potential characteristics

Notably, evoked potentials were observed during stimulation from the transverse sinus. Clear cortical activation was observed (figure 4). Subdural ECoG recordings showed stimulus-locked responses with increasing amplitude as pulse width and injected charge were raised. At higher intensities, two consistent peaks emerged: an early P40 (∼40–50 ms) and a later N100 (∼90–100 ms), similar in latencies to cortico-cortical evoked potentials (CCEPs) [21]. Both components scaled with stimulation intensity, producing biphasic responses up to ∼200 μV peak-to-peak.

3.4. Spatial distribution of neural activation

Topographical mapping of evoked potentials showed distinct spatial patterns following endovascular stimulation from the transverse sinus adjacent to the cerebellum (figure 5). Early positive peaks (∼40 ms) and later negative deflections (80–120 ms) were strongest over lateral electrodes, where AUC values exceeded 800 μV·ms. The heatmap revealed a focal region of maximal activity (∼1 cm^2), with a sharp amplitude gradient to neighboring electrodes. Spatial analysis showed a centroid-to-peak distance of 1.3 mm and a spatial spread of 2.5 mm, consistent with a focal distribution of cortical evoked responses. Strongest

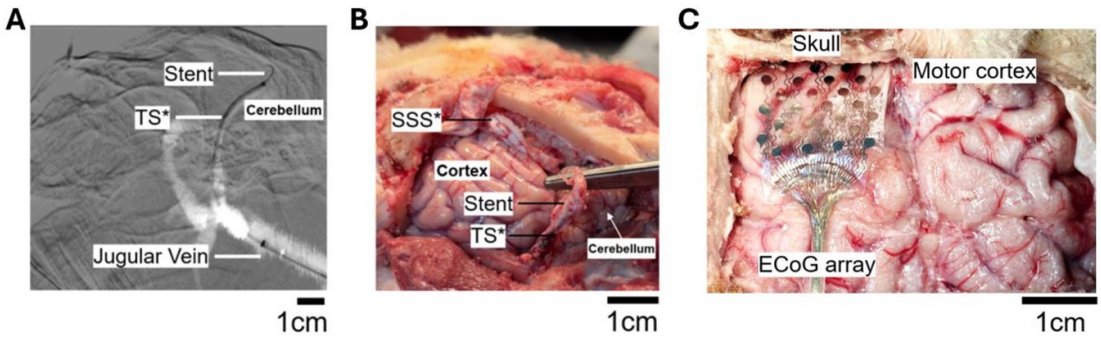

Figure 3. (A) Intraoperative digital subtraction angiography (DSA) confirming successful deployment of the stent-electrode array within the transverse sinus (TS*), showing unobstructed venous flow and proximity to the cerebellar structures. (B) Post-mortem anatomical exposure verifying accurate anatomical positioning of the device within the transverse sinus (TS*) and adjacent to the cerebellum. SSS stands for Superior Sagittal Sinus. (C) ECoG electrode placement on the sheep motor cortex.

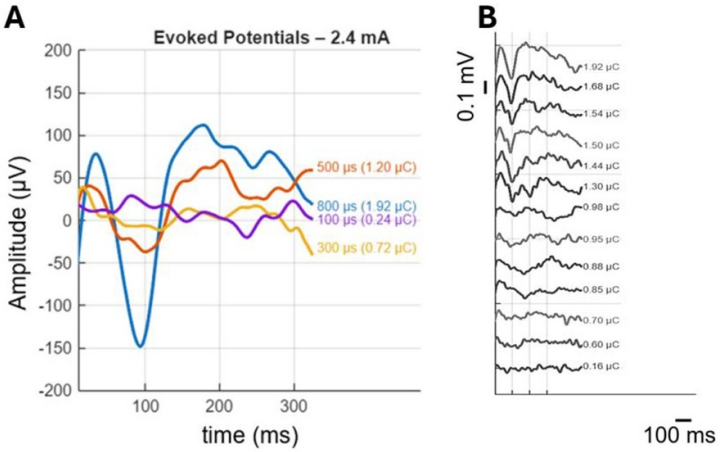

Figure 4. Evoked cortical potentials recorded from a representative channel following endovascular stimulation at varying charge levels. Each trace represents a single trial corresponding to a unique combination of stimulation amplitude (mA) and pulse width (μs), with the resulting charge (μC) labeled accordingly. (A) Stimulation was delivered at a fixed current amplitude (2.4 mA) with increasing pulse widths (100, 300, 500, and 800 μs), showing a clear charge-dependent increase in evoked response amplitude. (B) Traces are ordered by descending charge and vertically offset for clarity. A consistent waveform morphology is observed at higher charges, while lower charges yield reduced amplitude and altered temporal profiles.

responses were seen over the motor and somatosensory cortices.

3.5. Strength-duration relationship of stimulation near the cerebellum

Strength–duration analyses revealed quantifiable stimulation thresholds across all six implanted animals with endovascular electrodes implanted in the transverse sinus adjacent to the cerebellum (figure 6). Threshold current decreased with increasing pulse width (100–800 μs) and was described by the Lapicque model for all animals (figure 6(A)), yielding rheobase currents on the order of ∼1–2 mA and chronaxie values in the few-hundred microsecond range. While absolute thresholds showed some inter-subject variability, the convergence of curves at longer pulse widths suggests underlying neural excitability was relatively stable across the cohort. Inter-animal variability was observed in stimulation thresholds (figure 6). To investigate potential sources of this variability, a retrospective analysis of post-implantation venograms was performed (supplementary figure S1).

Conversion to charge per phase showed a gradual increase with increasing pulse width (figure 6(B)), reflecting the expected current–duration trade-off. Notably, analysis of charge density versus charge per phase revealed that stimulation in Animals 1, 2, and 4 resulted in charge densities below the Shannon safety limit across all stimulation parameters (figure 6(C)). However, data from Animals 3, 5, and 6 exceeded the limit at higher pulse widths (figure 6(C)). This was likely due to slightly more distal placement of the endovascular stent in these animals, where electrode contact was less direct as the device did not pass through the bone foramen. This resulted in greater current attenuation due to the low conductivity of the skull, and consequently higher stimulation thresholds

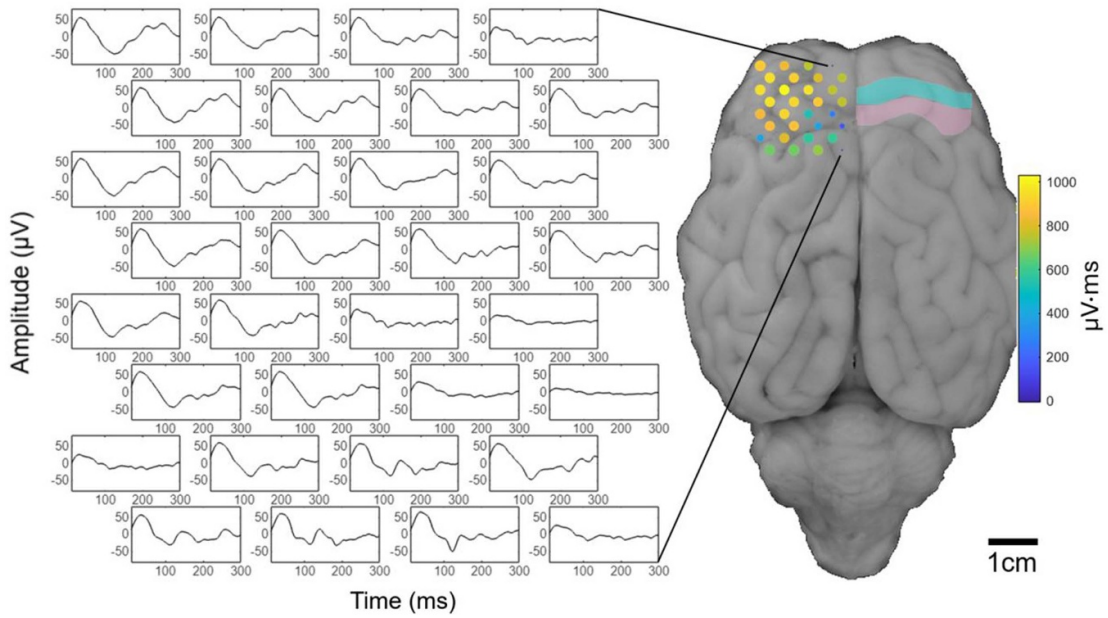

Figure 5. Evoked potentials recorded using a 32-channel ECoG grid following endovascular stimulation near the cerebellum (1 mA, 800 μs biphasic pulses, 0.498 Hz). The grid was placed ipsilateral to the stimulation site. Motor and somatosensory cortices were highlighted by cyan and pink respectively. Each subgraph corresponds spatially to electrode locations indicated by colored dots (color bar corresponds to area under curve) on an illustrative sheep cortical model based on surgical targeting and anatomical landmarks. Prominent responses at 40 ms and 100 ms post-stimulation were consistently observed across multiple electrodes, suggesting motor cortex activation.

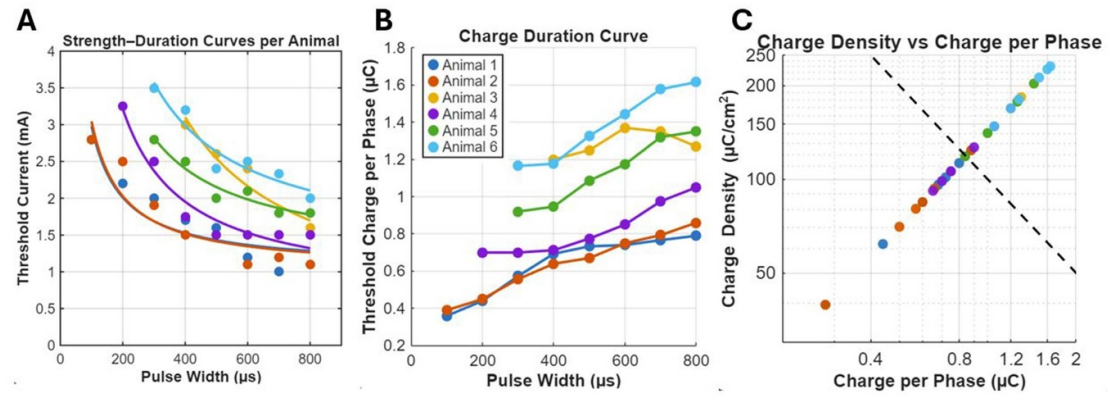

Figure 6. (A) Strength duration curves for Animals 1–6 with stent implanted near the cerebellum. Data points show minimum current to elicit an evoked potential at different pulse width, the data is fitted by Curve lines using the Lapicque formula. (B) Charge duration curve for the animals converted from the strength duration data points. Dots are connected by straight lines to visualize the trend. (C) Charge density versus charge per phase. Dotted line showed Shannon model coefficient $k = 2$. Left bottom zone represent safe zone with no tissue damage. Animals 3, 5, and 6 had threshold charge densities of 169 μC cm^{-2}, 118 μC cm^{-2}, and 148 μC cm^{-2}, respectively. Animals 1, 2, and 4 had thresholds between 39 and 92 μC cm^{-2}.

to evoke cortical response as seen in the left panel.

Table 1 summaries the rheobase and chronaxie values from fitting the data of the six animals. Rheobase currents ranged over 0.29–1.23 mA, with five of six subjects clustering near 1 mA. The single outlier (Animal 3, 0.29 mA) was associated with a proportionally longer chronaxie (see table 1). These results show that endovascular stimulation near the cerebellum may reliably evoke cortical responses using the designed pulse widths and charge levels.

3.6. Signal repeatability and stability

The signal to noise properties were quantified to establish the minimum requirements for reliable detection. As shown in figure 7, the characteristic waveform morphology (positive peak ~40 ms, negative peak ~100 ms) emerged clearly with increasing numbers of averaged trials. The characteristic positive (~40 ms) and negative (~100 ms) peaks became clearer with increasing trial counts, with 30 epochs still showing more noise than 50 or 75. Quantitative analysis revealed that the correlation with the grand average (75 trials) reached 0.86 after 30 trials and

Table 1. Rheobase and chronaxie values of endovascular stimulation.

Animal	Rheobase (mA)	Chronaxie (μs)
1	1.04	190
2	1.01	200
3	0.29	3820
4	0.69	730
5	1.15	440
6	1.23	570

exceeded 0.91 after 50 trials. Concurrently, the SNR improved from 3.7 dB (30 trials) to 6 dB (70 trials). These results indicate that while a minimum of 30 repetitions is required for dependable response detection, averaging over 50–70 trials provides substantially improved waveform fidelity and SNR for detailed analysis.

4. Discussion

This study provides the first strength-duration characterization of endovascular stimulation near the cerebellum, establishing rheobase and chronaxie parameters in an ovine model ($n = 6$). Stent-electrode arrays positioned in the transverse sinus elicited cortical potentials with latencies comparable to previously observed cortical conduction [21]. Beyond evoked responses, structural and electrochemical analyses highlighted features that support effective charge injection and stable tissue incorporation, which are relevant to chronic device performance. Collectively, these findings establish quantitative thresholds for endovascular stimulation, provide insight into the electrode-tissue interface, and offer a foundation for developing minimally invasive, long-term neuromodulation strategies targeting deep brain structures.

4.1. Positioning within neuromodulation modalities

Endovascular stimulation occupies a distinct niche between invasive and non-invasive neuromodulation modalities. Compared with deep brain stimulation (DBS), the endovascular approach avoids craniotomy and durotomy, substantially reducing surgical invasiveness and associated risks. Unlike parenchymal DBS, where electrodes are placed directly within compact neural targets, endovascular stimulation is delivered from within the vasculature and therefore occurs across a greater electrode-to-neural tissue distance. This difference in stimulation geometry is expected to influence activation thresholds and strength–duration characteristics. In contrast to transcranial direct current stimulation (tDCS), endovascular electrodes bypass skull-induced attenuation and spatial dispersion, enabling more efficient and focal intracranial current delivery.

The measured chronaxie (426 $\pm$ 236 μs) were more overlapped with reported ranges for subdural cortical stimulation (chronaxie: ~200–380 μs) [22, 23] than with effective stimulation thresholds derived for nuclear DBS targets, which typically exhibit shorter chronaxies (~129–151 μs) [24]. This similarity suggests that the excitation characteristics of endovascular stimulation are more comparable to those reported for subdural cortical stimulation than for parenchymal DBS. However, chronaxie alone does not identify the specific neural elements recruited and should not be interpreted as evidence for activation of a particular neuronal population or pathway. These findings provide a quantitative benchmark for comparison with established neuromodulation modalities and support the interpretation that the parameters of endovascular stimulation more closely resemble subdural cortical stimulation.

The longer chronaxie and intravascular electrode location may imply higher stimulation thresholds compared with parenchymal DBS systems. Because endovascular electrodes are separated from neural tissue by vessel wall layers, greater current amplitudes may be required to achieve comparable activation, increasing energy demands and limiting spatial selectivity. In contrast, DBS electrodes positioned within compact fiber tracts can achieve lower activation thresholds and highly focal recruitment, which may be advantageous for disorders requiring precise circuit targeting. Nevertheless, the endovascular approach may be advantageous when broader network engagement is desired, although the present study does not establish which neural circuits are preferentially recruited. Furthermore, avoidance of craniotomy and parenchymal penetration may provide a meaningful safety advantage in anatomically challenging posterior fossa targets.

4.2. Physiological mechanisms

Evoked potentials recorded over motor cortex exhibited early (40–50 ms) and late (90–100 ms) components comparable to the engagement of cerebellothalamocortical pathways or other polysynaptic cortical and brainstem pathways. These responses were strongest for electrodes on the motor and somatosensory cortex (figure 5). The early (40–50 ms) component falls within the window expected for polysynaptic recruitment of the cerebellothalamocortical projection or parallel brainstem pathways, potentially involving relay through the ventrolateral thalamus. The late (90–100 ms) component, may be through additional reticular and cortico-cortical loops before reaching motor and somatosensory cortex. Similar latency ranges have been reported following invasive cerebellar stimulation in humans and animals, where cortical motor responses typically emerge tens of milliseconds after cerebellar activation [25–28].

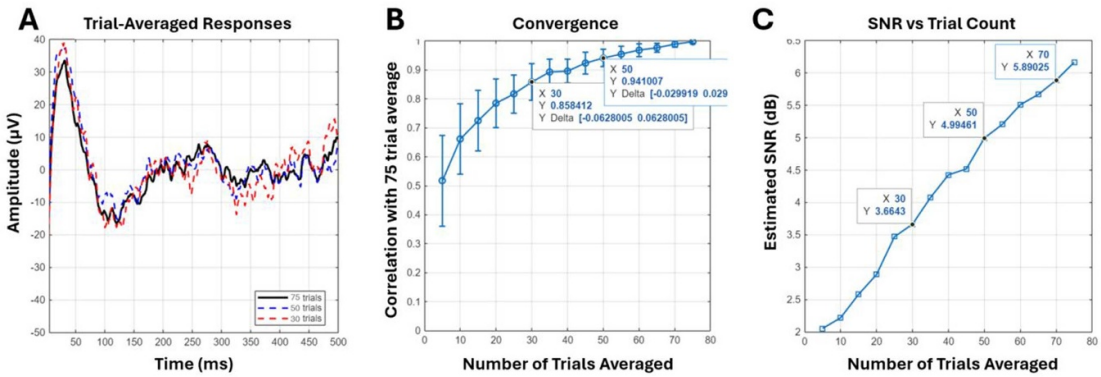

Figure 7. Effect of trial averaging on evoked potential detection. (A) Trial-averaged responses from 30, 50, and 75 epochs. (B) Correlation of subset averages with the 75-epoch reference. (C) Signal-to-noise ratio (SNR) as a function of number of epochs, showing improved reliability with increased averaging.

These latencies exceed direct corticocortical or corticospinal conduction times (<20 ms) [29], supporting a trans-synaptic mechanism rather than stimulus artifact or direct cortical excitation. A stimulus artifact or purely volume-conducted response would be expected within the first few milliseconds and would not produce two temporally distinct, physiologically plausible peaks. The presence of separable early and late components therefore supports a physiologically mediated, trans-synaptic response and is consistent with—but does not independently establish—recruitment of the cerebellar efferent system.

Anatomical and stimulus-parameter data provide further support for the interpretation that electrode position relative to the targeted cerebellar region influenced stimulation efficiency. Post-mortem analysis confirmed that the stimulating electrodes lay within the transverse sinus, anatomically adjacent to the cerebellar region. Retrospective analysis of the implantation venograms further demonstrated inter-animal differences in stent advancement within the transverse sinus (supplementary figure S1). Animals with either relatively distal implantation (Animal 3) or relatively proximal implantation (Animals 5 and 6) required higher stimulation currents to elicit cortical evoked potentials than animals with intermediate implantation positions (figure 6). This pattern suggests that deviation from an intermediate or potentially more favorable implantation position may have increased the distance or altered the spatial relationship between the active electrodes and the neural structures responsible for the cortical response.

Because the electrode-to-neural-target distance could not be measured directly, this retrospective positional analysis does not establish a monotonic distance–threshold relationship or demonstrate causality. Nevertheless, the dependence of stimulation threshold on implantation position would not be expected for a fixed stimulus artifact and supports the interpretation that the responses resulted from recruitment of neural structures located near the implanted electrodes.

While not definitive, the anatomical targeting, position-dependent variation in stimulation threshold, physiologically plausible response latencies, and distribution of the cortical responses collectively support the inference that stimulation likely recruited cerebellar tissue or cerebellar-associated pathways, producing evoked responses over the motor and somatosensory cortices.

However, the present experiments cannot definitively establish cerebellar-specific activation or determine which neural elements were initially recruited. Confirmation of a cerebellar origin would require additional pathway-specific evidence, such as simultaneous intracerebellar recordings, reversible pharmacological inactivation of the cerebellum, or another intervention demonstrating attenuation or abolition of the cortical responses when the cerebellar pathway is disrupted. It therefore remains possible that activation arose from the cerebellar cortex, deep cerebellar nuclei, cerebellar efferent fibers, adjacent brainstem or fiber pathways, dural or vascular afferents, or nearby cortical structures such as the visual cortex. Future studies combining precise three-dimensional electrode localization, computational modeling of the electric-field distribution, and pathway-specific electrophysiological or pharmacological testing will be required to determine the relative contribution of these potential activation pathways.

4.3. Translational study considerations

Charge density estimates revealed critical inter-animal variability. Three of six animals (3, 5, and 6) exceeded Shannon's safety limit ($k = 2$) at activation threshold, requiring 169 μC cm^{-2}, 118 μC cm^{-2}, and 148 μC cm^{-2}, respectively. Animals 1, 2, and 4 remained within limits (39–92 μC cm^{-2}). For context, previous chronic studies demonstrated no electrode corrosion or neuron loss up to 100 μC cm^{-2}

in cochlear implants [30]. While the presented values were comparable to this, chronic vascular and neural tissue response requires dedicated investigation before human application. Charge density calculations typically assume a single electrode's area. In a common cathode four-electrode array, current is shared across contacts, potentially reducing local charge density compared with bipolar configuration. Prior multielectrode studies suggest this distribution lowers per-contact charge requirements, although exact values depend on geometry and tissue properties [31]. More work is required to assess and optimize device safety in the aspect of charge injection, including increased geometric surface area of the electrode and alternative coatings (PtIr, IrOx, and PEDOT).

4.4. Limitations and future work

This acute terminal study is limited by the lack of histopathological validation of safety margins and biophysical modeling of current distribution. Addressing this will require chronic implantation studies ($\geqslant$90 d) with histological assessment of vascular integrity and glial response, combined with finite element modeling to ensure safe charge densities. Furthermore, the ovine cerebellum exhibits less cortical folding than human anatomy, and differences in skull thickness and CSF volume may affect current shunting. This highlights the need for patient-specific modeling to optimize electrode placement for human translation. Electrode placement in this study was constrained by vascular anatomy rather than optimized for minimal distance to targets, which could be improved in future designs through refined vascular access or alternative routes. The small sample size ($n = 6$) limits statistical power and generalizability, necessitating larger studies to confirm reproducibility and quantify variability. Moreover, the use of percutaneous pulse generators introduces infection risk, which could be mitigated in future chronic applications through wireless pulse generation.

No overt stimulation-related motor responses or adverse physiological changes were observed under general anaesthesia across the stimulation parameters investigated, including in animals with electrode misplacement. However, these acute experiments were not designed to systematically assess off-target neural activation or establish stimulation safety margins. Furthermore, general anaesthesia limited the assessment of behavioral or perceptual effects. Future studies should combine imaging-guided electrode localization with awake behavioral assessment and computational modeling of electric-field distributions to characterize stimulation selectivity, potential activation of adjacent structures, and safety at higher stimulation intensities.

Future work may explore the application of this endovascular approach for both diagnostic and therapeutic purposes in neurological disorders, such as epilepsy [32–36] and Parkinson's disease [37]. Extending the methodology to additional brain regions via alternative vascular access routes may enable investigation of other deep brain targets [38, 39]. In addition, translation to human studies remains an important long-term objective, particularly for conditions with limited treatment options, including severe epilepsy and treatment-resistant depression. Overall, this work provides an initial framework for further evaluation of minimally invasive endovascular neuromodulation strategies.

4.5. The future of Endovascular Neuromodulation

Endovascular neuromodulation occupies an intermediate position between non-invasive and surgically implanted stimulation modalities. Compared with DBS, it avoids craniotomy and parenchymal penetration while maintaining closer proximity to deep neural targets than TMS. Similar to vagus nerve stimulation and other peripheral nerve approaches, endovascular stimulation has the potential to engage distributed central networks rather than isolated focal structures. However, the present study evaluated only stimulation-evoked cortical potentials and does not establish functional modulation or therapeutic effects.

Recent work has demonstrated the feasibility of intravascular neural interfaces for stimulation and recording, establishing the vascular space as a viable access route [40–42]. The present study may extend this framework to endovascular stimulation adjacent to the cerebellum, suggesting that endovascular stimulation can reliably evoke cortical responses, as reflected by chronaxie values comparable to subdural cortical stimulation. However, further studies are required to determine the specific anatomical pathways responsible for these responses.

Endovascular systems are unlikely to replace established modalities such as DBS, which offers superior focal precision, but may provide a minimally invasive alternative when anatomical access is limited or when broader network engagement is desirable. Defining its clinical role will require further optimization of stimulation efficiency, mechanistic characterization of neural recruitment, off-target stimulation controls, computational modeling, demonstration of functional outcomes, and long-term safety evaluation.

5. Conclusion

This study presents the first strength–duration characterization of cortical evoked potentials elicited by endovascular stimulation delivered near the cerebellum in an ovine model. Strength–duration analysis provided rheobase and chronaxie estimates, offering endovascular stimulation parameter selection and comparison with established intracranial stimulation

approaches. These results support further investigation in neuromodulation applications.

Acknowledgments

This research was funded by the Japan Science and Technology Agency's Moonshot Research and Development Program (JPMJMS2012). Device fabrication was performed in part at the Melbourne Centre for Nanofabrication (MCN) in the Victorian Node of the Australian National Fabrication Facility (ANFF). Animal studies were performed at the labs of the Florey Institute of Neuroscience and Mental Health, relied on the support and contributions of Joel Villalobos, Huakun Xin, Tom Vale, Quan Nguyen, and Miranda Marcon.

Data availability statement

All data that support the findings of this study are included within the article (and any supplementary files).

Implantation position analysis available at https://doi.org/10.1088/1741-2552/ae998c/data1.

Author contributions

Weijie Qi 0000-0002-0686-4948
Conceptualization (lead), Data curation (lead), Formal analysis (lead), Investigation (lead), Methodology (lead), Project administration (lead), Validation (lead), Visualization (lead), Writing – original draft (lead), Writing – review & editing (lead)

Joel Villalobos 0000-0003-3417-7720
Conceptualization (equal), Data curation (equal), Formal analysis (supporting), Investigation (equal), Methodology (equal), Project administration (equal), Supervision (equal), Validation (equal), Visualization (supporting), Writing – review & editing (equal)

Jingyang Liu 0000-0002-3329-9796
Conceptualization (equal), Formal analysis (supporting), Investigation (supporting), Methodology (supporting), Resources (equal), Validation (equal), Visualization (supporting), Writing – review & editing (equal)

Huakun Xin
Data curation (supporting), Formal analysis (supporting), Investigation (supporting), Methodology (equal), Resources (supporting), Validation (equal), Visualization (supporting), Writing – review & editing (equal)

Martin J Spencer 0000-0002-2001-9054
Formal analysis (supporting), Methodology (equal), Validation (supporting), Visualization (supporting), Writing – review & editing (equal)

Sepehr Kazemi
Formal analysis (supporting), Methodology (equal), Validation (supporting), Visualization (supporting), Writing – review & editing (supporting)

Stella Ho 0000-0003-2876-2077
Conceptualization (supporting), Formal analysis (supporting), Validation (supporting), Visualization (supporting), Writing – review & editing (supporting)

Joseph West 0000-0003-1676-2758
Formal analysis (supporting), Methodology (supporting), Supervision (supporting), Validation (supporting), Visualization (supporting), Writing – review & editing (supporting)

David B Grayden 0000-0002-5497-7234
Conceptualization (equal), Formal analysis (supporting), Funding acquisition (lead), Investigation (supporting), Methodology (supporting), Project administration (supporting), Resources (equal), Software (equal), Supervision (lead), Validation (supporting), Visualization (supporting), Writing – review & editing (equal)

Sam E John 0000-0003-3780-2210
Conceptualization (equal), Formal analysis (supporting), Funding acquisition (lead), Investigation (supporting), Methodology (supporting), Project administration (supporting), Resources (equal), Software (equal), Supervision (lead), Validation (supporting), Visualization (supporting), Writing – review & editing (equal)

References

[1] Nicolelis M A L 2022 Brain–machine–brain interfaces as the foundation for the next generation of neuroprostheses *Natl Sci. Rev.* **9** nwab206
[2] Woeppel K, Yang Q and Cui X T 2017 Recent advances in neural electrode–tissue interfaces *Curr. Opin. Biomed. Eng.* **4** 21–31
[3] Falowski S M, DiLorenzo D J, Shannon L R, Wallace D J, Devries J, Kellogg R G, Cozzi N P, Fogg L F and Byrne R W 2015 Optimizations and nuances in neurosurgical technique for the minimization of complications in subdural electrode placement for epilepsy surgery *World Neurosurg.* **84** 989–97
[4] Fountas K N and Smith J R 2007 Subdural electrode-associated complications: a 20-year experience *Stereotact. Funct. Neurosurg.* **85** 264–72
[5] Shi L, Sun Y, Chen L, Xue H, Zhang W and Yang H 2019 Diagnosis and treatment of a penetrating brain injury caused by a welding electrode: a case report *Medicine* **98** e14528

[6] Soldozy S, Young S, Kumar J S, Capek S, Felbaum D R, Jean W C, Park M S and Syed H R 2020 A systematic review of endovascular stent-electrode arrays, a minimally invasive approach to brain-machine interfaces *Neurosurg. Focus* **49** E3
[7] Mitchell P *et al* 2023 Assessment of safety of a fully implanted endovascular brain-computer interface for severe paralysis in 4 patients *JAMA Neurol.* **80** 270
[8] Oxley T J *et al* 2021 Motor neuroprosthesis implanted with neurointerventional surgery improves capacity for activities of daily living tasks in severe paralysis: first in-human experience *J. NeuroInterv. Surg.* **13** 102–8
[9] Tai C-H and Tseng S-H 2022 Cerebellar deep brain stimulation for movement disorders *Neurobiol. Dis.* **175** 105899
[10] Koch G *et al* 2019 Effect of cerebellar stimulation on gait and balance recovery in patients with hemiparetic stroke: a randomized clinical trial *JAMA Neurol.* **76** 170–8
[11] Yao Q, Tang F, Wang Y, Yan Y, Dong L, Wang T, Zhu D, Tian M, Lin X and Shi J 2022 Effect of cerebellum stimulation on cognitive recovery in patients with Alzheimer disease: a randomized clinical trial *Brain Stimul.* **15** 910–20
[12] Stroud A, Tisch S and Jonker B P 2022 Cerebellar cortex stimulation for acquired dystonia: a case report and review of its role in modern surgical practice *Stereotact. Funct. Neurosurg.* **100** 321–30
[13] Yamao Y, Matsumoto R, Kikuchi T, Yoshida K, Kunieda T and Miyamoto S 2021 Intraoperative brain mapping by cortico-cortical evoked potential *Front. Hum. Neurosci.* **15** 635453
[14] Tai Y D, John S E, Xin H, Grayden D B, Unnithan R and Widdicombe B, "Wireless endovascular device", Australian Provisional Patent Application No. 2025903006 (filed 14 July 2025)
[15] Harris A R, Grayden D B and John S E 2023 Electrochemistry in a two- or three-electrode configuration to understand monopolar or bipolar configurations of platinum bionic implants *Micromachines* **14** 722
[16] Oxley T J *et al* 2016 Minimally invasive endovascular stent-electrode array for high-fidelity, chronic recordings of cortical neural activity *Nat. Biotechnol.* **34** 320–7
[17] Oxley T J *et al* 2017 An ovine model of cerebral catheter venography for implantation of an endovascular neural interface *J. Neurosurg.* **128** 1020–7
[18] Gerboni G *et al* 2018 Cortical brain stimulation with endovascular electrodes *2018 40th Annual Int. Conf. of the IEEE Engineering in Medicine and Biology Society (EMBC)* (IEEE) pp 3088–91
[19] Wong Y T, Chen S C, Seo J M, Morley J W, Lovell N H and Suaning G J 2009 Focal activation of the feline retina via a suprachoroidal electrode array *Vision Res.* **49** 825–33
[20] Harris A R, Ruslim M, Xin H, Shen Z, Liu J, Spencer T, Garrett D, Grayden D B and John S E 2025 Endovascular neural stimulation with platinum and platinum black modified electrodes *Sci. Rep.* **15** 9676
[21] Matsumoto R, Nair D R, LaPresto E, Bingaman W, Shibasaki H and Lüders H O 2007 Functional connectivity in human cortical motor system: a cortico-cortical evoked potential study *Brain* **130** 181–97
[22] Abalkhail T M *et al* 2017 Intraoperative direct cortical stimulation motor evoked potentials: stimulus parameter recommendations based on rheobase and chronaxie *Clin. Neurophysiol.* **128** 2300–8
[23] Perlmutter J S and Mink J W 2006 Deep brain stimulation *Annu. Rev. Neurosci.* **29** 229–57
[24] Reich M M, Steigerwald F, Sawalhe A D, Reese R, Gunalan K, Johannes S, Nickl R, Matthies C, McIntyre C C and Volkmann J 2015 Short pulse width widens the therapeutic window of subthalamic neurostimulation *Ann. Clin. Transl. Neurol.* **2** 427–32
[25] Mottolese C, Richard N, Harquel S, Szathmari A, Sirigu A and Desmurget M 2013 Mapping motor representations in the human cerebellum *Brain* **136** 330–42
[26] Ugawa Y, Uesaka Y, Terao Y, Hanajima R and Kanazawa I 1995 Magnetic stimulation over the cerebellum in humans *Ann. Neurol.* **37** 703–13
[27] Daskalakis Z J, Paradiso G O, Christensen B K, Fitzgerald P B, Gunraj C and Chen R 2004 Exploring the connectivity between the cerebellum and motor cortex in humans *J. Physiol.* **557** 689–700
[28] Popa T, Velayudhan B, Hubsch C, Pradeep S, Roze E, Vidailhet M, Meunier S and Kishore A 2013 Cerebellar processing of sensory inputs primes motor cortex plasticity *Cereb. Cortex* **23** 305–14
[29] Lemon R N 2008 Descending pathways in motor control *Annu. Rev. Neurosci.* **31** 195–218
[30] Shepherd R K, Carter P M, Enke Y L, Wise A K and Fallon J B 2019 Chronic intracochlear electrical stimulation at high charge densities results in platinum dissolution but not neural loss or functional changes in vivo *J. Neural Eng.* **16** 026009
[31] Cogan S F, Ludwig K A, Welle C G and Takmakov P 2016 Tissue damage thresholds during therapeutic electrical stimulation *J. Neural Eng.* **13** 021001
[32] Stieve B J, Richner T J, Krook-Magnuson C, Netoff T I and Krook-Magnuson E 2023 Optimization of closed-loop electrical stimulation enables robust cerebellar-directed seizure control *Brain* **146** 91–108
[33] Iwata N K and Ugawa Y 2005 The effects of cerebellar stimulation on the motor cortical excitability in neurological disorders: a review *Cerebellum* **4** 218–23
[34] Kros L, Eelkman Rooda O H J, De Zeeuw C I and Hoebeek F E 2015 Controlling cerebellar output to treat refractory epilepsy *Trends Neurosci.* **38** 787–99
[35] Salam M T, Perez Velazquez J L and Genov R 2016 Seizure suppression efficacy of closed-loop versus open-loop deep brain stimulation in a rodent model of epilepsy *IEEE Trans. Neural Syst. Rehabil. Eng.* **24** 710–9
[36] Wathen C A, Frizon L A, Maiti T K, Baker K B and Machado A G 2018 Deep brain stimulation of the cerebellum for post-stroke motor rehabilitation: from laboratory to clinical trial *Neurosurg. Focus* **45** E13
[37] Koch G, Brusa L, Carrillo F, Lo Gerfo E, Torriero S, Oliveri M, Mir P, Caltagirone C and Stanzione P 2009 Cerebellar magnetic stimulation decreases levodopa-induced dyskinesias in Parkinson disease *Neurology* **73** 113–9
[38] Rajah G, Saber H, Singh R and Rangel-castilla L 2018 Endovascular delivery of leads and stentrodes and their applications to deep brain stimulation and neuromodulation: a review *Neurosurg. Focus* **45** E19
[39] Teplitzky B A, Connolly A T, Bajwa J A and Johnson M D 2014 Computational modeling of an endovascular approach to deep brain stimulation *J. Neural Eng.* **11** 026011
[40] Liu J, Yang X, Musmar B and Hasan D M 2025 Transarterial approach for neural recording and stimulation: present and future *J. Clin. Neurosci.* **135** 111180
[41] Liu J, Grayden D B, Keast J R, Booth L C, May C N and John S E 2024 Feasibility of endovascular stimulation of the femoral nerve using a stent-mounted electrode array *J. Neural Eng.* **21** 036034
[42] Liu J, Grayden D B, Keast J R and John S E 2024 Endovascular stimulation of the pudendal nerve using a stent-mounted electrode array *J. Neural Eng.* **21** 046047